2024 IEEE/RSJ International Conference on Intelligent Robots and Systems (IROS)
October 14-18, 2024. Abu Dhabi, UAE

Real-time terrain assessment and Bayesian-based path planning for off-road navigation

Tianwei Niu[1], Shuwei Yu, Liang Wang, Haoyu Yuan, Shoukun Wang[2]*, Junzheng Wang[3]

***Abstract*— In the context of unstructured and unknown environment, the autonomous navigation still faces many challenges, such as assessing rough terrain and deciding how to safely navigate complex terrain. In this work, we propose a robust and practical off-road navigation framework that has been successfully deployed on a vibroseis truck for land exploration. First, in degraded wild scenes, a tightly coupled lidar-GNSS-inertial fusion odometry and mapping framework is adopted to construct a local point cloud map around the vehicle in real-time and provide precise localization. Then, based on amplitude-frequency characteristic analysis and point cloud PCA, a multi-layer terrain assessment map containing terrain roughness, obstacles and slope information is obtained. Finally, combining Gaussian distribution based adaptive sampler and Bayesian sequentially updated proposal distribution, a local graph is efficiently built to obtain multiple path solutions under constrained conditions. Both simulations and field experiments show that the proposed navigation framework can decide how to travel on a flat road even in harsh terrain conditions, naturally suppressing frequent attitude angle changes and preventing vehicle accidents.**

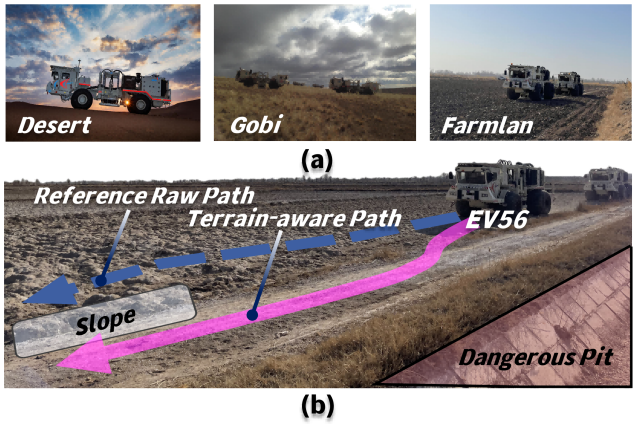

Fig. 1: (a) Operating environments. (b) Characteristics of field vehicles path planning.

I. INTRODUCTION

Autonomous field vehicles are widely used in various fields such as agriculture, disaster relief, mining, and land exploration, providing significant economic and social value [1]. Unlike structured roads, vehicle navigation in unknown outdoor environments emphasizes terrain risk perception and making optimal decisions [2]. Fig.(1) shows the operational scenario and path planning characteristics of vibroseis truck EV56 [3]. Before operation, EV56 is provided with a surveyed reference path. To drive on flatter roads and avoid intense changes in attitude angles, the navigation system should first analyze the roughness and slope of the ground and dangerous areas in surrounding environment. Then, based on the acquired environmental information, how the navigation system efficiently generates an optimal path under constrained conditions is also a great challenge.

The outdoor terrain assessment is considered a prerequisite for safe and efficient navigation on unstructured road. In numerous works, terrain traversability analysis can generally be divided into two main categories: those based on either 3D point clouds [4][5] or image data [6][7]. In the context of outdoor navigation, 2.5D digital elevation maps (DEM) [8] are the most commonly used simple map representations. DEM can be constructed using depth sensors, containing elevation information around the vehicle. Wermelinger et al. [9] analyze the slope, ruggedness, and elevation changes of terrain based on generated 2.5D maps to derive traversal costs. Furthermore, similar statistical quantification methods, such as Gaussian mixture models [10] and principal component analysis (PCA) [11], are also widely studied in terrain estimation. Jian et al. [12] utilize point cloud fitting methods to assess the roughness of small planes. Chen et al. [7] proposed a fast, compact, and motion-robust ontology-aware terrain classification method. This method integrates an ontology-based terrain classification model with a CNN model based on visual input (terrain appearance), further enhancing the accuracy of terrain classification. Path planning algorithms for navigating complex outdoor terrain have always been a key technology in outdoor navigation, especially for rovers used in planetary exploration. Ono et al. [13] employ machine learning to perceive potential risks from image data. Then, they generate paths for Mars rovers based on the rapid-exploration random graph and the A* algorithm. These paths consider the risk associated with wheel placement, ensuring smooth execution of rover tasks. The algorithm classifies all risky terrain as non-traversable areas, limiting the vehicle's ability to escape from constrained conditions. The Grand Challenge hold by Defense Advanced Research Projects Agency (DARPA) over a decade ago led to significant breakthroughs in autonomous navigation in desert environments [14][15]. The sampling-based motion planning

*Corresponding authors: Shoukun Wang.

This work was supported by the National Natural Science Foundation of China [Grant 62173038]

[1]Tianwei Niu is with the Localization and Motion Planning, School of Automation, Beijing Institute of Technology, 100081 Beijing, China [1]tywin_niu@163.com

[2]Shoukun Wang and [3]Junzheng Wang are with the State Key Laboratory of Intelligent Control and Decision of Complex System, School of Automation, Beijing Institute of Technology, 100081 Beijing, China [2]bitwsk@bit.edu.cn, [3]wangjz@bit.edu.cn

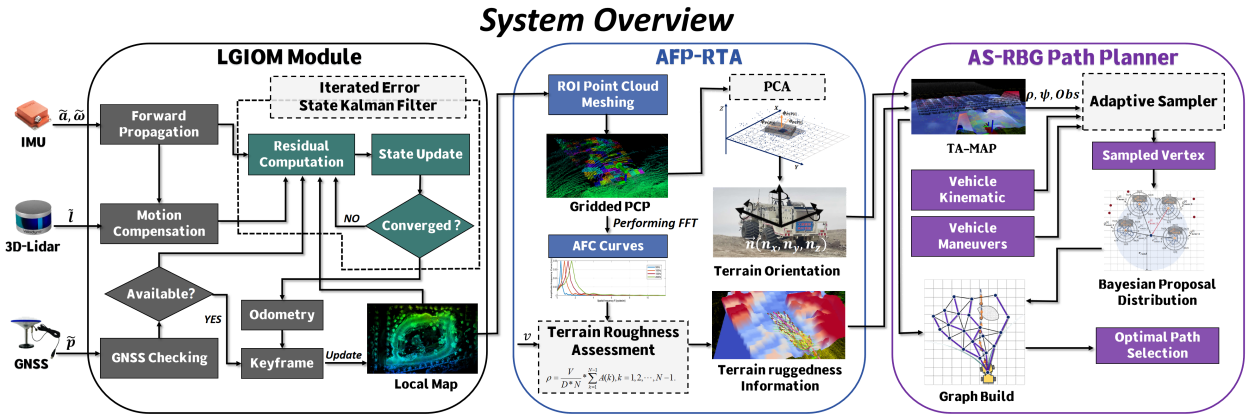

Fig. 2: System overview.

approach was extensively utilized in this challenge because it's comprehensive coverage of the surrounding terrain. Xiao et al. [16] proposed a data-driven approach to learn an inverse kinodynamic model for high-speed navigation in unstructured terrain. This method is capable of capturing complex vehicle kinodynamic models and environmental information based on onboard inertial observations, enabling rapid and reliable responses in unstructured environments. Meng et al. [17] also introduced a learning-based method, the TerrainNet visual perception system, and used the MPPI planner with perceived terrain features for local planning. TerrainNet utilizes multi-view RGB image information to accomplish semantic and geometric terrain prediction for aggressive, off-road navigation. Then, at each planning time step, the MPPI planner performs 3000 rollouts using the kinematic model, estimating the cost of terrain features for each rollout to obtain the optimal trajectory. This approach utilizes end-to-end terrain perception techniques, which are known to require large training datasets. Meanwhile, the trajectories generated by the MPPI planner are prone to getting trapped in local minima, which can be fatal in outdoor environments.

In this work, a novel and practical framework is proposed to address vehicle navigation in unknown and unstructured environments, as shown in Fig. (2). The main contributions made in this work are as follows:

- Based on terrain geometry information, we proposed a new framework to continuously quantify terrain roughness using the characteristics of the terrain amplitude-frequency.
- A Gaussian-based adaptive sampler considering terrain information, vehicle behavior, and kinematic constraints, is designed to generate biased sampling points.
- Based on Bayesian sequential update proposal distribution, we significantly improved the quality and success rate of vertex expansion under constrained conditions.

II. System Overview

The system architecture proposed in this paper is shown in Fig. (2). The system mainly consists of three modules: 1) a tightly-coupled lidar-GNSS-inertial Odometry and Mapping framework (LGIOM), 2) a real-time terrain assessment framework based on amplitude-frequency characteristics and point cloud PCA (AFP-RTA), and 3) an adaptive sampler and rapid-exploring Bayesian graph (AS-RBG) based path planner.

In the LGIOM module, the iterated error-state Kalman filter algorithm is adopted to tightly fuse IMU data, lidar points, and GNSS measurements, which achieves precise state estimation and mapping. The implementation of the LGIOM module follows the approach outlined in [18], which is not discussed in detail in this paper due to limited space.

The AFP-RTA module receives the local map constructed in real-time by LGIOM, and extracts the point cloud of the regions of interest (ROI). Then, the point cloud is first employed for assessing roughness based on amplitude-frequency characteristics, and second, they are used for analyzing slope and obstacle information of the terrain. The above information is integrated into a multi-layer terrain assessment map (TA-MAP) used for autonomous navigation.

Finally, the adaptive sampler integrates information from TA-MAP, vehicle kinematics, vehicle maneuver prediction to efficiently generate reasonable sampling points. Based on observations of past extending results, each vertex sequentially Bayesian updates its proposal distribution $\mathcal{Q}_i$, thereby efficiently building high-quality local graph $\mathcal{G}_L$ in constrained environments. Then, the A* algorithm is employed to compute the optimal path set traversing flat terrain.

III. Real-time Terrain Assessment Based on Amplitude-Frequency Characteristics and Point Cloud PCA

Before the local point cloud map from LGIOM is analyzed, two preprocessing steps are required: 1) extraction of the ROI point cloud, and 2) partitioning of the ROI point cloud into patches, as shown in Fig.(3). Compared to the local point cloud map, the extracted ROI point cloud avoids analyzing areas that are either too far from the vehicle or beyond the kinematic limit. Additionally, the resolution of the PCP decreases as the distance from the vehicle grows. This is partly because vehicles have higher requirement for

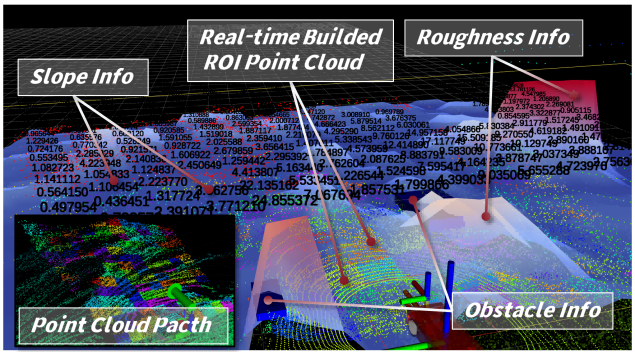

Fig. 3: Multi-layer terrain assessment map (TA-MAP). The left bottom corner is the point cloud patches.

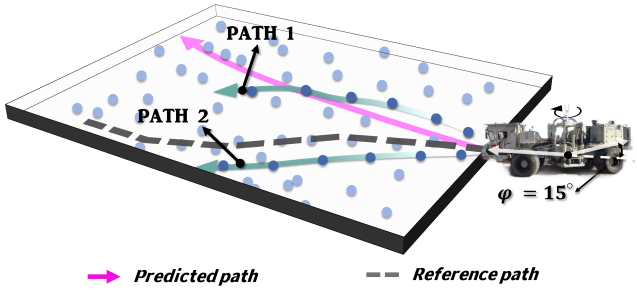

Fig. 4: Alternative path selection under different emphases.

roughness resolution in the near range than in the distance. On the other hand, as the LiDAR points naturally become more sparse the farther they are from the vehicle, a larger PCP size can bring more precise analysis results.

The z-values of the PCP_i are used to form the signal sequence $\mathcal{Z}_i$ of terrain profile. Performing fast Fourier transform (FFT) on $\mathcal{Z}_i$ yields the spatial frequency response $\mathcal{F}_i$ of the terrain. The normalized amplitude $A(k)$ of $\mathcal{F}_i$ can be calculated by

$$A(k) = \begin{cases} \frac{|\mathcal{Z}_i(k)|}{N}, k = 0 \\ \frac{|\mathcal{Z}_i(k)|}{(N/2)}, k = 1, 2, \cdots, N-1 \end{cases}, \tag{1}$$

where N is the length of the signal. $|\mathcal{Z}_i(k)|$ represents taking the modulus of k-th complex numbers to obtain the amplitude.

The distribution range of the signal frequency can be calculated by

$$f(k) = k\frac{f_{Samp}}{N}, k = 0, 1, 2, \cdots, N-1, \tag{2}$$

where $f(k)$ is the actual frequency corresponding to the k-th amplitude value, and f_{Samp} is the sampling frequency of the point cloud.

The sub-frequency components in the AFC curve can reflect the small-scale terrain features. Consequently, in this work, the terrain roughness will be quantified by the envelope area of the AFC curve relative to the sub-frequency component, calculated by

$$\rho = \sum_{k=1}^{N-1}(A(k)\frac{f_{Samp}}{N}) = \frac{f_{Samp}}{N}\sum_{k=1}^{N-1}A(k). \tag{3}$$

The terrain analysis should take into account both the spatial characteristics of the terrain and mechanical impact on vehicles. In terms of mechanical impact, the higher speed of the vehicle on the same uneven road, the stronger the impact on the vehicle. Thus, the quantification of terrain relative roughness should be correlated with the vehicle's speed. Assuming the point cloud sampling interval is D and the vehicle speed is V, the sampling frequency f_{Samp} can be calculated by

$$f_{Samp} = \frac{1}{T} = \frac{1}{D/V} = \frac{V}{D}. \tag{4}$$

Ultimately, the relative roughness of the terrain can be calculated by

$$\rho = \frac{V}{\mu_t DN}\sum_{k=1}^{N-1}A(k), \tag{5}$$

where μ_t is the tire size factor. All PCP_i in the ROI point cloud will undergo roughness quantification in the aforementioned pipeline and be saved to the TA-MAP $\mathbb{M}_{\text{M-TA}}$. In this work, the surface normal vector $[n_x, n_y, n_z]$ of each PCP_i will be obtained by PCA. The terrain attitude information in the TA-MAP provides the motion planner with a more comprehensive consideration of traversal costs.

IV. Adaptive Sampler Considering Vehicle Maneuvers and Terrain Features

A. Gaussian distributed sampling point generation

As shown in Fig.(4), when the vehicle continues driving in the current state (steering angle 15°), it is more likely to take PATH1 instead of PATH2. When considering that the vehicle should stay as close as possible to the reference path, PATH2 is preferred over PATH1. Therefore, this paper combines two Gaussian distributions $\mathcal{N}_{RP}\left(\mu_{RP}, \sigma^2_{RP}\right)$ and $\mathcal{N}_{PP}\left(\mu_{PP}, \sigma^2_{PP}\right)$ with one uniform distribution U_{RP} to generate adaptive sampling points. $\mathcal{N}_{RP}$ ensures that sampling points become dense near the reference path, $\mathcal{N}_{PP}$ makes more sampling points distribute around the predicted path, and U_{RP} ensures the randomness of sampling points.

Firstly, given the vehicle's position (x_{ego}, y_{ego}), steering angle δ_{ego}, and forward sampling distance d_{sap}, reference path section $\mathcal{P}_{ref}$ and the curve $\mathcal{T}$ predicting the future position of the vehicle is obtained. n key points $P^{[i]}_{key}$ will be obtained at equal intervals on $\mathcal{P}_{ref}$, as shown in Fig.(5). At $P^{[i]}_{key}$, sampling will be conducted with $P^{[i]}_{key}$ as the origin. Then, the Gaussian distribution $\mathcal{N}_{RP}$ and $\mathcal{N}_{PP}$ will be applied only in the y-direction, while the x-direction follows a uniform distribution. The expression of the probability density function is

$$\begin{cases} f_{unif}(y) &= p_{unif}(y) \\ f_{nor}(x) &= \frac{1}{\sqrt{2\pi\sigma^2}}\exp\{-\frac{(x-\mu)^2}{2\sigma^2}\} \end{cases}, \tag{6}$$

where $f_{nor}(x)$ denotes probability density functions of a Gaussian distribution with mean μ and variance σ. $\mathcal{N}_{RP}$ and $\mathcal{N}_{PP}$ will be assigned different parameters (μ and σ).

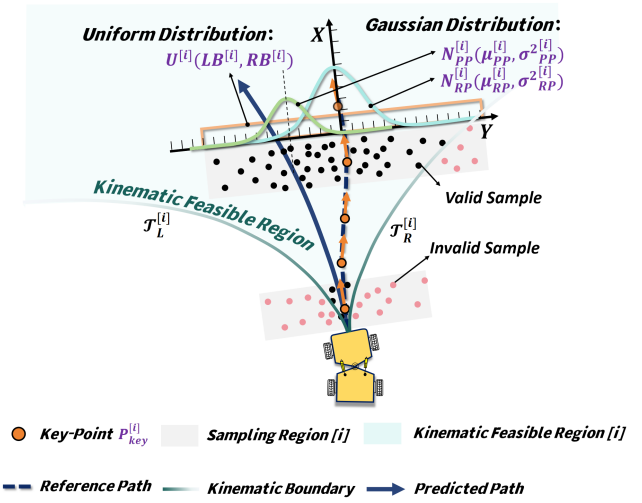

Fig. 5: Adaptive sampler based on Gaussian distribution and vehicle maneuvers.

$\mu = \lambda_\mu \delta_{ego}$ is used to distribute more sampling points along the desired direction, where λ_μ is the steering coefficient. In $\sigma = \lambda_\sigma r_0$, r_0 represents the distance between the current key point and the vehicle, while λ_σ is the distance factor. $\sigma = \lambda_\sigma r_0$ ensures that the sampling strategy can increase the sampling range as the distance from the vehicle increases, which aligns with the vehicle kinematics, as shown in Fig.(5).

B. Avoid sampling in restricted areas

The validity check in this study primarily considers two factors: obstacles and vehicle maneuver limitations. To generate collision-free paths, obstacle interference detection [19] needs to be completed during each sampling step. The obstacles is obtained through image-based segmentation method [20] and obstacles are considered threatening only if their height is greater than one-third of the tire diameter.

Since EV56 is a non-holonomic constraint system, sampling points should be avoided from being generated within the kinematically infeasible region. Based on the kinematic model in [21], with the current articulation angular velocity $\dot{\gamma}$ and vehicle speed v_f as inputs, the kinematic feasible region can be determined, as shown in Fig.(5).

C. More sampling points in flat terrain

Vehicles operating in unstructured environments are expected to travel on flatter roads. TA-MAP provides the terrain roughness information around the vehicle, allowing for generating more sampling points in areas with lower roughness. Once the highest and lowest roughness $\rho_{\max}$, $\rho_{\min}$ within the current vehicle's field of view are obtained, we define

$$k(\rho) = \begin{cases} 0 & \rho \geqslant \rho_{\max} \\ \frac{\rho - \rho_{\min}}{\rho_{\max} - \rho_{\min}} & \rho \leqslant \rho_{\max} \end{cases}, \tag{7}$$

where $k(\rho)$ outputs a value between 0 and 1. Then, generator $rand()$ is responsible for generating random numbers υ between 0 and 1, where $\upsilon \sim U(0,1)$. Finally, the trigger

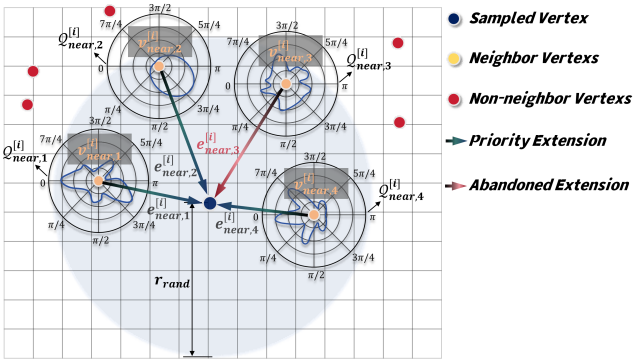

Fig. 6: Local graph vertex extension based on Bayesian sequential proposal distribution.

$\upsilon \sim U(0,1)$ is designed to determine whether to adopt the sampling point s_i, defined as

$$\mathrm{T} = \begin{cases} 1, & \upsilon > k(r) \\ 0, & \text{else} \end{cases}. \tag{8}$$

When $\mathrm{T} = 1$, the sampling point is adopted; otherwise, it is removed.

V. Rapidly-exploring Bayesian Graph based Path Planning

A. Local graph building

When each sampling point $s_{rand} = [x_{rand}, y_{rand}]^T$ is generated, the vertex in the graph obtained by $v_{rand} = \mathbb{M}_{\text{M-TA}}(s_{rand})$, where $v_{rand} = [x_{rand}, y_{rand}, \rho_{rand}, \psi_{rand}]^T$ and ψ_{rand} is the slope value.

First, the vertex set $\mathcal{V}_{near}$ within a distance radius r_{rand} from the vertex v_{rand} are obtained using kd-tree search, as shown in Fig.(6). Each vertex v_i existing in the graph $\mathcal{G}_L$ will sequentially update and establish its proposal distribution $\mathcal{Q}_i(d|d^{[i-1]}, \mathcal{D}_j^{[i]})$. Here, $d^{[i-1]}$ represents the successful extension between parent vertex v_{i_parent} and v_i, and $\mathcal{D}_j^{[i]}$ represents the set of j samples containing both successful and failure extensions of vertex v_i towards other vertexes in $\mathcal{V}_{near}$. The Bayesian learning scheme is adopted to adaptively update $\mathcal{Q}_i$, which learns from past samples to improve the success rate of vertex extensions. The $\mathcal{Q}_i$ will follow $\pi_{posterior} \propto \rho_{\text{prior}} \cdot \lambda_{likelihood}$.

The von Mises-Fisher distribution ($\boldsymbol{Vmf}$) is chosen as the prior distribution $\pi_{posterior}$, which has been proven to be well-suited for circular normal distributions [22], defined as

$$\boldsymbol{Vmf}(x|\mu,\kappa) = C_p(\kappa) e^{\kappa \mu^T x}, \tag{9}$$

where μ is the mean direction and κ is the concentration parameter. Eq.(9) defines the distribution on $(p-1)$-sphere in $\mathbb{R}^p$. The normalization constant $C_p(\kappa)$ is defined as

$$C_p(\kappa) = \frac{\kappa^{p/2-1}}{(2\pi)^{p/2} I_{p/2-1}(\kappa)}, \tag{10}$$

where I_p is p-order modified Bessel function.

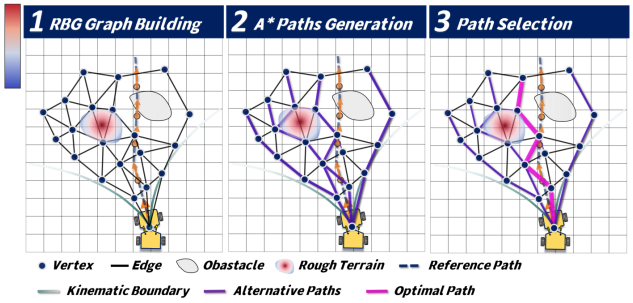

Fig. 7: RBG based path generation process.

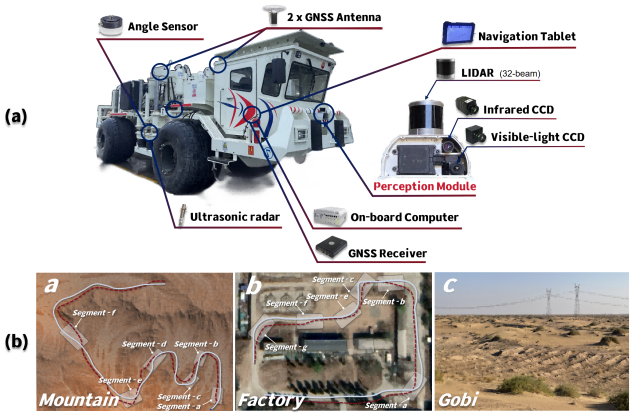

Fig. 8: Vibroseis truck with autonomous navigation hardware and experimental scenarios.

This prior distribution concentrates the probability density distribution on the direction of successful extension $d^{[i-1]}$. Next, this prior distribution ***Vmf*** will be combined with the periodic kernel function $pk(\cdot)$ [23] to generate a sequential Bayesian updating scheme. As a likelihood estimation function, the $pk(\cdot)$ will sequentially update its parameters based on the failed and successful samples (including quality factors) at step j. Finally, the $\mathcal{Q}_i$ can be defined as

$$\mathcal{Q}_i(d|d^{[i-1]},\mathcal{D}_j^{[i]}) = \begin{cases} Vmf_p(x|\mu,\kappa) & j=1 \\ \frac{\mathcal{Q}_i(d|d^{[i-1]},\mathcal{D}_{j-1}^{[i]})P_{SeqUpd}(d,d_{j-1}^{[i]})}{\delta_j} & j>1, \end{cases} \tag{11}$$

and $P_{SeqUpd}(d, d_{j-1}^{[i]})$ is given by

$$P_{SeqUpd}(d,d_{j-1}^{[i]}) = \begin{cases} \left(1-pk\left(d,d_{j-1}^{[i]}\right)\right) & d_{j-1}^{[i]} \in \mathcal{D}_{fail}^{[i]} \\ pk\left(d,d_{j-1}^{[i]}\right) & d_{j-1}^{[i]} \in \mathcal{D}_{succ}^{[i]}, \end{cases} \tag{12}$$

where δ_j can ensure that $\mathcal{Q}_i$ integrates to 1 over its domain.

The periodic kernel function can be expressed as

$$pk(d,d') = \tau \exp\left(-\frac{2\sin^2(\pi|d-d'|/p)}{l^2}\right), \tag{13}$$

where l is the length scale. $p = 2\pi$ is the periodicity parameter. The parameter $0 < \tau < 1$ is the scaling factor. For failed samples, $\tau = 0.85$; while for successful samples, τ is dynamically adjusted depending on the edge quality.

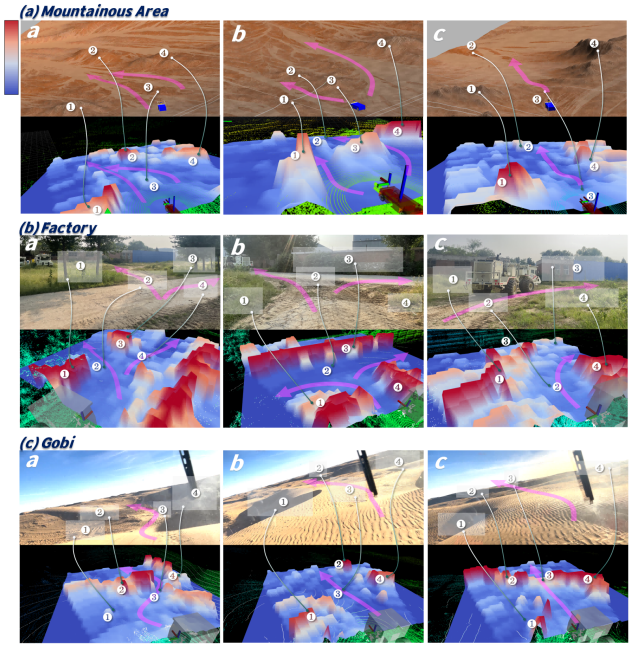

Fig. 9: Terrain assessment map by AFP-RTA.

At i-step exploration, we obtain all nodes $\mathcal{V}_{near}^{[i]} = \{v_{near,1}^{[i]}, v_{near,2}^{[i]}, ..., v_{near,n}^{[i]}\}$ near the vertex v_i. In these directions extending from the neighbor vertexes to v_i, we prioritize the directions with higher probabilities, as shown in Fig.(6). When there are more than three successful extension edges, the next vertex is sampled for future exploration. The above process continues until the number of nodes or edges reaches the limit $N_{\mathcal{V},\max}$, $N_{\mathcal{E},\max}$.

B. Graph based alternative paths generation

In the local graph $\mathcal{G}_L(\mathcal{V},\mathcal{E})$, $\mathcal{V}$ represents the vertex set, while $\mathcal{E}$ represents the set of edges with weights including length, traversal cost, and deviation cost. In Fig.(7), the A* algorithm is employed to generate alternative paths from the current position of the vehicle (root vertex) to the leaf vertexes. Different from traditional A* algorithms, in this work, vertexes and edges incorporate considerations of roughness and slope, ensuring the generation of shorter paths that traverse flatter terrain. Ultimately, the equivalent weight of the path is expressed as

$$\boldsymbol{Weight}_{\text{EWM}}(\mathcal{P}_i) = w_L L_{sum} + w_\rho \rho_{sum} + w_\psi \psi_{sum}, \tag{14}$$

where L_{sum}, ρ_{sum} and ψ_{sum} represent the length weight, the roughness weight and the attitude change weight respectively. w_L, w_ρ and w_ψ are corresponding coefficients.

Finally, the A* algorithm calculates the optimal path $\mathcal{P}_{opt}^{[i]} = \left\{v_0^{[i]}, v_1^{[i]}, ..., v_n^{[i]}, L_{sum}^{[i]}, \rho_{sum}^{[i]}, \psi_{sum}^{[i]}\right\}$ from each leaf vertex to the root vertex. Among all the optimal paths $\mathcal{AP}$, the one with the minimum cost is selected.

After the aforementioned algorithmic process, as illustrated in Fig.(7), an optimal path from the vehicle to a specific leaf vertex is obtained. The final path is smoothed by iterative optimization [24] based on cubic spline.

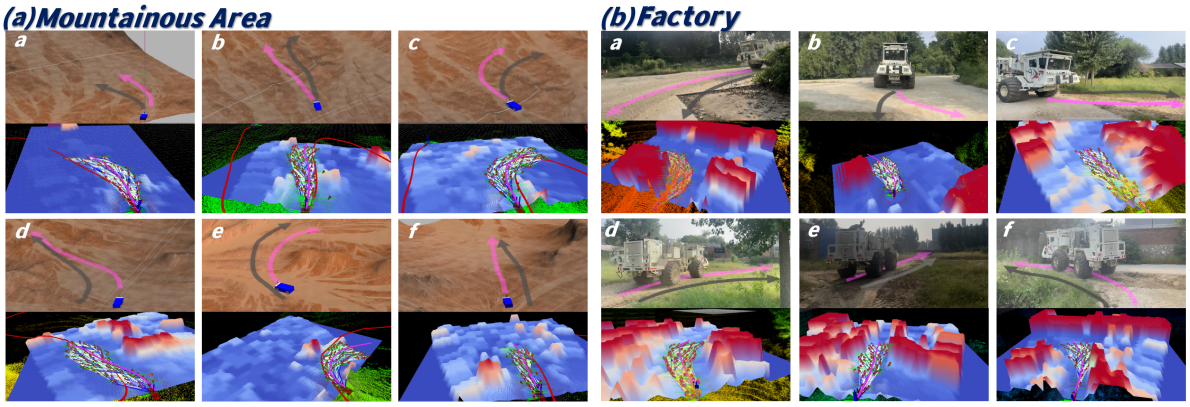

Fig. 10: AS-GBP Planner navigating the EV56 in off-road scenarios.

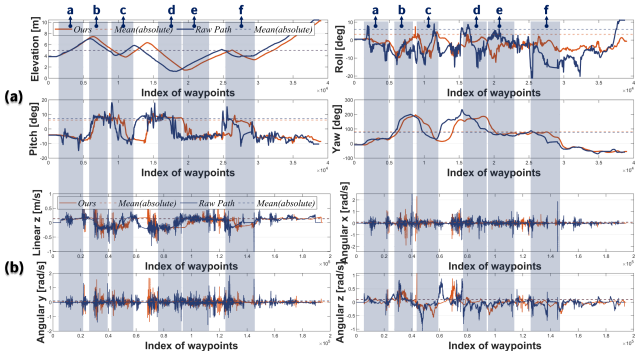

Fig. 11: Comparison of the vehicle's attitude angle and its acceleration when adopting the path planned by the proposed method and the reference path.

VI. Experiments and Results

In this section, the method validation will be conducted based on both simulation and field experiments. The experiments will be conducted on the EV56 vibroseis truck, which is equipped with multiple sensors, as shown in Fig.(8).(a), including Lidar, Radar, GPS and other sensors. The proposed framework are implemented by C++, which were executed on an on-board computer Nuvo-7160GC.

A. Terrain assessment performance

The column a in Fig.(8).(b) shows the world in the simulator, which is located in a rugged mountainous area with many large rocks, mounds of soil, and slopes. The column b in Fig.(8).(b) depicts a comprehensive experimental scene located in the backyard of a factory area in Hebei, China. It comprises dirt roads, concrete roads, cobblestone roads, walls, and construction equipment. The scene depicted in column c of Fig.(8).(b) is a typical Gobi desert.

The ROI point cloud is fed into the AFP-RTA in real-time at 10Hz. The terrain analysis results are shown in Fig.(9). The first and second rows of sub-figure in Fig.(9) show environmental information and the TA-MAP derived from AFP-RTA, respectively. The terrain roughness is visualized using a gradient color scheme, where light blue represents the lowest roughness and red represents the highest roughness.

In Fig.(9).(a) column a, AFP-RTA demonstrates excellent discrimination of different roughness levels on the ground. This allows the vehicle not only to perceive the rugged terrain but also to distinguish where it is more rugged. In column b, the vehicle can accurately identify flat areas (although narrow) even in severely restricted terrain, which can increase the vehicle's ability to escape. In column c, upcoming slope areas are also categorized as higher roughness, allowing the vehicle to make decisions such as slowing down in advance.

The experimental results of EV56 driving in the factory area are shown in Fig.(9).(b). In column a, the vehicle accurately identifies flat roads located to the left and right side. For the trees and ground protrusions in ① and ③, the TA-MAP indicates high roughness. In column b, AFP-RTA identifies the wall ③ and indicates the highest roughness. Meanwhile, the flat cement road surface ② is also accurately recognized. In column c, as the vehicle travels on the dirt ground, it provides the flat area ahead.

Fig.(9).(c) shows the experimental results of EV56 driving in the Gobi. In column a, although the vehicle is navigating through a highly restricted environment, AFP-RTA successfully identifies the navigable flat road ③. In column b, the large pit located to the left of the vehicle is assigned the highest roughness estimate by AFP-RTA, preventing potential rollover accidents. In column c, although there is a horizontally rough section ②-③-④ ahead of the vehicle, the vehicle must traverse this section. It can be seen in TA-MAP that ③, as a terrain with lower roughness (relative to ②④), is accurately identified as the "breakthrough point" for the vehicle.

B. Path planning performance in unstructured environments

The terrain analysis results mentioned above provide essential information for the subsequent path planning. The Fig.(10) shows the results of path planning for the vehicle in two different environments. In order to stay as close to the guidance of the reference path while navigating through flat roads, the AS-GBP planner made some intelligent detour decisions, resulting in a slight increase in path length, which can be seen in Fig.(8).(b).

The left sub-figure of Fig.(10) shows the optimal decisions

made by the path planner in real-time in the mountainous environment (the video can be found in the supplementary files). The adaptive sampler in Sec.(IV) results in: 1) more sampling points falling in flat areas (column a, b, c, e, f), 2) biased generation of sampling points based on the current vehicle behavior and kinematic constraints (column b, c, e), and 3) guided sampling paths in flat regions by the reference path (column e). In comparison to the reference path, the path planned by the AS-RBG planner does not traverse rough terrain or protruding hillsides, as the reference path does. Instead, it selects flat road near the raw path. The AS-RBG's decision avoids larger and more abrupt changes in attitude, as shown in Fig.(11).

Similarly, in the factory setting, the proposed planner adopted by EV56 demonstrated good performance. The vehicle is able to navigate under complex scenarios while staying on flat roads, as observed in right sub-figure of Fig.(10). In column a, the planned path avoids the dirt road shown in the image, opting instead for the cement road. Similar decision-making is demonstrated in column b. In column c, the vehicle found the flat path from the cement road to the dirt road despite the presence of trees on both sides. Similarly, in column d, e, and f, compared to the reference path, the planner generated paths that pass through flat areas, ensuring the vehicle's safe travel within the factory.

VII. CONCLUSIONS

In this work, a novel and practical navigation framework is proposed that is applicable to unknown and unstructured environments. This framework has been successfully deployed on the vibroseis EV56 truck used for oil extraction. First, a tightly-coupled multi-sensor fusion and mapping scheme is designed to ensure robust localization and real-time precise mapping. The roughness and slope of terrain are obtained by amplitude-frequency analysis and point cloud PCA, respectively, and then saved into multi-layer terrain assessment map. Then, an adaptive sampler based on Gaussian distribution considers multiple key factors to generate biased sampling points. Finally, a local graph containing Bayesian proposal distributions for each vertex is adopted to generate terrain-aware alternative paths. Extensive simulations and field experiments were conducted in various environments, which showed that the vehicle is capable of autonomously navigating through unstructured terrain.

REFERENCES

[1] N. Melenbrink, J. Werfel, and A. Menges, "On-site autonomous construction robots: Towards unsupervised building," *Automation in construction*, vol. 119, p. 103312, 2020.

[2] Z. Chen, J. Li, S. Wang, J. Wang, and L. Ma, "Flexible gait transition for six wheel-legged robot with unstructured terrains," *Robotics and Autonomous Systems*, vol. 150, p. 103989, 2022.

[3] T. Niu, L. Wang, Y. Xu, J. Wang, and S. Wang, "Quintic bézier curve and numerical optimal solution based path planning approach in seismic exploration," *Control Engineering Practice*, vol. 145, p. 105855, 2024.

[4] A. Sinha and P. Papadakis, "Mind the gap: Detection and traversability analysis of terrain gaps using lidar for safe robot navigation," *Robotica*, vol. 31, no. 7, pp. 1085–1101, 2013.

[5] C. Ye and J. Borenstein, "T-transformation: Traversability analysis for navigation on rugged terrain," in *Unmanned Ground Vehicle Technology VI*, vol. 5422. SPIE, 2004, pp. 473–483.

[6] R. Manduchi, A. Castano, A. Talukder, and L. Matthies, "Obstacle detection and terrain classification for autonomous off-road navigation," *Autonomous robots*, vol. 18, pp. 81–102, 2005.

[7] Y. Chen, C. Rastogi, and W. R. Norris, "A cnn based vision-proprioception fusion method for robust ugv terrain classification," *IEEE Robotics and Automation Letters*, vol. 6, no. 4, pp. 7965–7972, 2021.

[8] S. Mukherjee, P. K. Joshi, S. Mukherjee, A. Ghosh, R. Garg, and A. Mukhopadhyay, "Evaluation of vertical accuracy of open source digital elevation model (dem)," *International Journal of Applied Earth Observation and Geoinformation*, vol. 21, pp. 205–217, 2013.

[9] M. Wermelinger, P. Fankhauser, R. Diethelm, P. Krüsi, R. Siegwart, and M. Hutter, "Navigation planning for legged robots in challenging terrain," in *2016 IEEE/RSJ International Conference on Intelligent Robots and Systems (IROS)*. IEEE, 2016, pp. 1184–1189.

[10] I. Miller and M. Campbell, "A mixture-model based algorithm for real-time terrain estimation," *Journal of Field Robotics*, vol. 23, no. 9, pp. 755–775, 2006.

[11] E. M. DuPont, C. A. Moore, and R. G. Roberts, "Terrain classification for mobile robots traveling at various speeds: An eigenspace manifold approach," in *2008 IEEE International Conference on Robotics and Automation*. IEEE, 2008, pp. 3284–3289.

[12] Z. Jian, Z. Lu, X. Zhou, B. Lan, A. Xiao, X. Wang, and B. Liang, "Putn: A plane-fitting based uneven terrain navigation framework," in *2022 IEEE/RSJ International Conference on Intelligent Robots and Systems (IROS)*. IEEE, 2022, pp. 7160–7166.

[13] M. Ono, T. J. Fuchs, A. Steffy, M. Maimone, and J. Yen, "Risk-aware planetary rover operation: Autonomous terrain classification and path planning," in *2015 IEEE aerospace conference*. IEEE, 2015, pp. 1–10.

[14] S. Thrun, M. Montemerlo, H. Dahlkamp, D. Stavens, A. Aron, J. Diebel, P. Fong, J. Gale, M. Halpenny, G. Hoffmann, *et al.*, "Stanley: The robot that won the darpa grand challenge," *Journal of field Robotics*, vol. 23, no. 9, pp. 661–692, 2006.

[15] D. Dolgov, S. Thrun, M. Montemerlo, and J. Diebel, "Path planning for autonomous driving in unknown environments," in *Experimental Robotics: The Eleventh International Symposium*. Springer, 2009, pp. 55–64.

[16] X. Xiao, J. Biswas, and P. Stone, "Learning inverse kinodynamics for accurate high-speed off-road navigation on unstructured terrain," *IEEE Robotics and Automation Letters*, vol. 6, no. 3, pp. 6054–6060, 2021.

[17] X. Meng, N. Hatch, A. Lambert, A. Li, N. Wagener, M. Schmittle, J. Lee, W. Yuan, Z. Chen, S. Deng, *et al.*, "Terrainnet: Visual modeling of complex terrain for high-speed, off-road navigation," *arXiv preprint arXiv:2303.15771*, 2023.

[18] W. Xu and F. Zhang, "Fast-lio: A fast, robust lidar-inertial odometry package by tightly-coupled iterated kalman filter," *IEEE Robotics and Automation Letters*, vol. 6, no. 2, pp. 3317–3324, 2021.

[19] G. v. d. Bergen, "Efficient collision detection of complex deformable models using aabb trees," *Journal of graphics tools*, vol. 2, no. 4, pp. 1–13, 1997.

[20] C. Deng, S. Wang, J. Wang, Y. Xu, and Z. Chen, "Lidar depth cluster active detection and localization for a uav with partial information loss in gnss," *Unmanned Systems*, 2024.

[21] T. Xu, Y. Shen, Y. Huang, and A. Khajepour, "Study of hydraulic steering process for articulated heavy vehicles based on the principle of the least resistance," *IEEE/ASME Transactions on Mechatronics*, vol. 24, no. 4, pp. 1662–1673, 2019.

[22] K. Mardia, "Distribution theory for the von mises-fisher distribution and its application," in *A Modern Course on Statistical Distributions in Scientific Work: Volume 1—Models and Structures Proceedings of the NATO Advanced Study Institute held at the University of Calgagry, Calgary, Alberta, Canada July 29–August 10, 1974*. Springer, 1975, pp. 113–130.

[23] A. J. Wathen and S. Zhu, "On spectral distribution of kernel matrices related to radial basis functions," *Numerical Algorithms*, vol. 70, no. 4, pp. 709–726, 2015.

[24] P. Krüsi, P. Furgale, M. Bosse, and R. Siegwart, "Driving on point clouds: Motion planning, trajectory optimization, and terrain assessment in generic nonplanar environments," *Journal of Field Robotics*, vol. 34, no. 5, pp. 940–984, 2017.